

Polydimethylsiloxane Foam-Based Fully 3D Printed Soft Pressure Sensors

Xenofon Karagiorgis, Gaurav Khandelwal, Ajay Beniwal, Radu Chirila, Peter J. Skabara, and Ravinder Dahiya*

Highly sensitive pressure sensors, with a wide operating range, are needed in applications such as wearables, prostheses, and haptic-based interactive systems. Herein, fully 3D printed capacitive pressure sensors comprising polydimethylsiloxane (PDMS) foam-based dielectric layer, sandwiched between the poly(3,4-ethylenedioxythiophene):polystyrene sulfonate and silver nanowire-based electrodes, are presented. The printed electrodes exhibit excellent electrical properties ($1.6 \Omega \text{ sq}^{-1}$, 20.35 kS m^{-1}) and bendability. Various ratios of PDMS to ammonium bicarbonate (NH_4HCO_3) are evaluated to obtain dielectric layer with optimum pore sizes for better performance and ease of fabrication. The device with a PDMS: NH_4HCO_3 ratio of 4:0.8 exhibits a linear response with a sensitivity of 0.0055 kPa^{-1} in the tested pressure range of 5–170 kPa. The fully 3D printed sensors also show excellent repeatability over 500 cycles with an average hysteresis of 1.53%, and fast response and recovery times of 89 and 195 ms, respectively. The superiority of the presented 3D printed foam-based device is confirmed by 30% higher sensitivity in comparison with PDMS-based sensors. Finally, as a proof-of-concept, the pressure sensors presented in this study are assessed for their suitability in underwater environments and touch-based object recognition.

1. Introduction

Pressure sensors have been gaining increasing interest due to their wide range of applications such as human motion monitoring, underwater vehicles, electronic skin (e-skin), robotics, prosthetics, and medical diagnostics.^[1–3] Given the wider applicability, often in human-centric applications, it is desirable to develop soft pressure sensors using simple fabrication processes and for accurate, sensible, and reproducible outcomes over a wide operating range from 1 to about 100 kPa, depending on the application.^[4,5] To meet these requirements, various sensing mechanisms have been explored for pressure sensing, including piezoresistive,^[6–10] piezoelectric,^[11–15] triboelectric,^[16–20] capacitive,^[21–24] etc. The latter has been investigated more because of good sensitivity, stability, shorter response times, and less susceptibility to noise, simple sensor structure that offers ease of fabrication, and simple readout electronics.^[4,25–29]


However, the conventional fabrication processes adopted so far to develop these sensors are tedious and time-consuming. Further, scalability of sensors for applications such as large areas electronic skin for the whole body of a robot^[30] is challenging. In this regard, a facile automated method such as additive manufacturing is desirable and has been explored in recent years. Further, addressing biodegradability and biocompatibility are the additional features^[31,32] that could also help to reduce electronic waste.^[33] In this direction, we reported recently the PDMS foam-based 3D printed capacitive sensors.^[34] Herein, the same multimaterial 3D printing technique was exploited to create biocompatible fully 3D printed capacitive pressure sensors for underwater monitoring and touch-based object recognition.

Tuning the properties of dielectric materials or modifying the sensor design can drastically improve the sensitivity and dynamic range of the pressure sensors and many attempts have been made.^[4] For example, PDMS-based elastomers and composites and polyurethane, etc. have been used as the soft dielectric layer to improve mechanical strength, stretchability, elasticity, and conformability.^[4,25,35–38] The dielectric properties of soft materials such as PDMS are not much influenced by temperature and humidity. At the same time, it is difficult to tune the density of

X. Karagiorgis, G. Khandelwal, A. Beniwal, R. Chirila
School of Engineering
University of Glasgow
Glasgow G12 8QQ, UK

X. Karagiorgis, P. J. Skabara
School of Chemistry
University of Glasgow
Glasgow G12 8QQ, UK

R. Dahiya
Bendable Electronics and Sustainable Technologies (BEST) Group
Northeastern University
Boston, MA 02115, USA
E-mail: r.dahiya@northeastern.edu

 The ORCID identification number(s) for the author(s) of this article can be found under <https://doi.org/10.1002/aisy.202300367>.

© 2023 The Authors. Advanced Intelligent Systems published by Wiley-VCH GmbH. This is an open access article under the terms of the Creative Commons Attribution License, which permits use, distribution and reproduction in any medium, provided the original work is properly cited.

DOI: 10.1002/aisy.202300367

these soft materials, which, in turn, limits the sensitivity of sensors based on them. This can be partly addressed by blending PDMS with high dielectric materials such as barium titanate,^[39] zirconium^[40] and ZnO nanowires,^[21] or porous structures.^[36,41] While blends of PDMS with other nanomaterials help to improve the sensitivity, it also lowers the softness, and eventually, a trade-off is needed.^[21] In this regard, porous PDMS could offer a better alternative as it improves both the softness and sensitivity.^[34,42] The porous PDMS is prepared either using sodium chloride,^[43–46] sugar/salt cubes,^[45,47–49] NH_4HCO_3 ,^[34,39,50,51] or potassium chloride.^[45,52] In light of this, to enhance comprehension of how the porous dielectric influences device performance, the impact of the PDMS to NH_4HCO_3 ratio was investigated. This examination aimed to gain a more profound understanding of the role played by the porous dielectric in device functionality.

2. Experimental Section

Sylgard 184 silicone elastomer kit (PDMS prepolymer and curing agent) was purchased from Dow Corning. NH_4HCO_3 , dimethyl sulfoxide (DMSO), and silver nanowires in 0.5% isopropyl suspension (aspect ratio: about 170) were purchased from Sigma–Aldrich. Polyethylene oxide (PEO), M_w : 1 000 000, was purchased from Alfa Aesar. Poly(3,4-ethylenedioxythiophene): polystyrene sulfonate (PEDOT:PSS), PH-1000, was purchased from Ossila Ltd.

2.1. Material Preparation

PDMS prepolymer was mixed with the curing agent (the weight ratio of prepolymer and curing agent is 10:1). After mixing, the PDMS was degassed to remove bubbles. The prepared PDMS was used for the encapsulation and the fabrication of the sensor using bulk PDMS as the dielectric layer. The porous PDMS was prepared by blending with different ratios of NH_4HCO_3 followed by stirring for 5 min. Three different ratios of PDMS: NH_4HCO_3 (4:0.8, 4:1, and 4:1.2) were selected for device fabrication. **Figure 1** illustrates the fabrication process for porous PDMS and electrode layers.

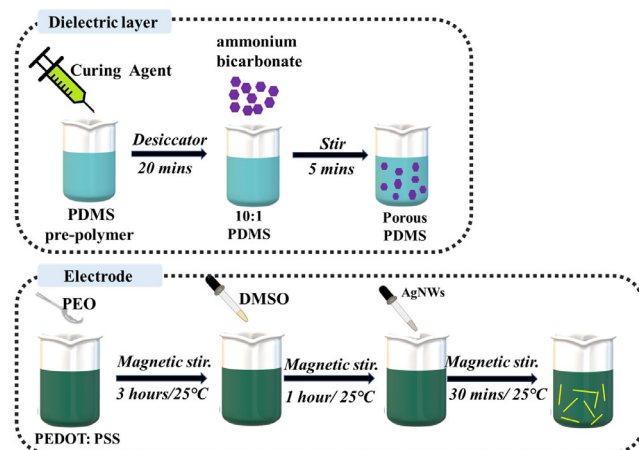


Figure 1. Schematic illustration of the preparation of materials for each layer.

The conductive ink was prepared using the steps explained in our previous work.^[34] Briefly, 1 wt% of biodegradable PEO was added to PEDOT:PSS and the solution was stirred at room temperature to obtain a water-based and easily printable ink of desired viscosity.^[53–55] Further, for better conductivity, 10% v/v of DMSO was added and the solution was stirred at room temperature for another hour until the ink became homogeneous. Finally, 2% v/v of silver nanowires (AgNWs) was added and the ink was stirred for 30 min at room temperature to obtain the uniform dispersion of the NWs, as depicted in Figure 1. AgNWs showed the highest conductivity among all metals ($6.3 \times 10^7 \text{ S m}^{-1}$ at 20°C).^[56]

2.2. Device Fabrication

Figure 2 illustrates the sensor design and its fabrication by DIW. The device consists of two electrodes that are 20 mm wide, 15 mm long, and 0.5 mm thick, and an extended square contact pad of 5 mm. The dielectric layer has the same design as the electrodes, but its thickness varies in regard to the ratio of PDMS: NH_4HCO_3 (**Table 1**). The devices were encapsulated with PDMS in a square shape of 30 mm \times 30 mm. The DIW printer (Brinter, Turku, Finland) utilizes a computer-controlled translation stage to print different patterns by extruding the ink through a nozzle. In turn, layers with controlled architecture and composition are developed. The top and bottom encapsulation layers were printed on a heated bed at 80°C . The PDMS was filled in a syringe with nozzle size 18G (internal diameter of 0.84 mm), and a pressure of 600 mbar was applied to print the layer. After the PDMS layer was cured, the syringe was filled with conductive ink in which 120 mbar was applied using a nozzle 21G (internal diameter of 0.51 mm). The porous PDMS layer was printed on top of the electrode using a 14G nozzle (internal diameter of 1.54 mm). Pressures of 3, 4, and 6 bar were applied to print the dielectric layers with different porosity (obtained with PDMS: NH_4HCO_3 ratios of 4:0.8, 4:1, and 4:1.2, respectively). A dielectric layer with a PDMS: NH_4HCO_3 ratio of 4:0.6 was printed but the concentration of NH_4HCO_3 was not sufficient to generate pores throughout the PDMS dielectric layer. We refer to the device with the porous layer based on PDMS: NH_4HCO_3 : 4:0.8 as D1 and likewise 4:1 as D2, and 4:1.2 as D3. The first three printed layers were directly transferred to a preheated oven for 1 h at 90°C to allow the pores to form. In the meantime, another layer of PDMS was printed with the same parameters as the first one. When it was cured, a layer of electrode was printed. Copper wires on the side of the top and bottom electrodes were attached with silver paste and epoxy to gain access to the device. The two structures (one with the porous layer and the other without) were eventually bonded with a thin film of PDMS on the corners.

2.3. Materials Characterization

The size of the pores in the dielectric layer was examined using an optical microscope (ECLIPSE LV100ND, Nikon) equipped with a digital camera (DS-Fi2, Nikon). The microscope was controlled using LAS EZ (Leica Application Suite, version 3.4.0, the Leica Microsystems Switzerland Limited), and the pictures were taken with 100 \times magnification. The sheet resistance of the

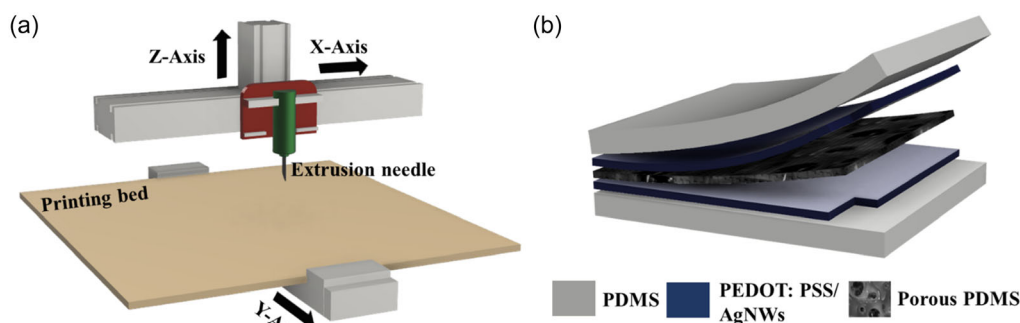


Figure 2. Schematic representation of a) DIW technique and b) printed capacitive pressure sensor.

Table 1. Summary of the characteristics of each capacitive pressure sensor based on the porous dielectric layer.

PDMS:NH ₄ HCO ₃	Average pore size [μm]	Thickness (<i>d</i>) [mm]	Dielectric constant (ϵ_r)	Sensitivity [kPa ⁻¹]
4:0.8	315	1.2 ± 0.2	1.246 ± 0.003	[5–170 kPa]: 0.0055
4:1	299	0.95 ± 0.2	1.388 ± 0.003	[5–225 kPa]: 0.0027
4:1.2	273	0.83 ± 0.2	1.498 ± 0.005	[5–190 kPa]: 0.0041

electrode was measured with four-point probe equipment (Ossila Ltd.). The probes were placed in line with equal spacing (0.5 cm). Electrical current was passed through two outer probes (1 and 4) and sheet resistance was obtained by measuring the change in the voltage. Scanning electron microscopy (SEM) (Nova NanoSEM 630, FEI) with an accelerating voltage of 10 kV was used to analyze the electrode's structure and morphology. The mechanical properties of the dielectric layers were characterized through a Sauter FH 10 Force Gauge and Sauter TVL manual test stand.

2.4. Device Characterization

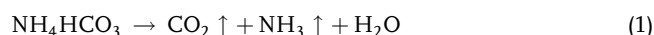
The capacitive pressure sensor was tested using a custom-made setup comprising a controllable linear motor, as depicted in Figure S1, Supporting Information. A square contactor with a circular dot was attached to the motor base to apply the force on the device. The contactor/load cell (1004 aluminum load cell) was controlled using the LabVIEW program. Furthermore, the load cell was calibrated by attaching the output to a voltmeter and we noted that 1.48 mV corresponds to 1 N. Here, the radius of the active area (the area of the sensor where the force was applied) is 0.5 cm. During sensor testing, forces from 0.15 to 20 N were applied, and the motor position was noted. Essentially, motor displacement corresponds to different applied forces.

3. Results and Discussions

The printed electrode exhibited conductivity of approximately 20 kS m⁻¹ and sheet resistance of around 1.6 Ω sq⁻¹ (Figure S2, Supporting Information). The optimized electrode exhibited a relatively low sheet resistance and displayed excellent bendability. Figure S3, Supporting Information, is an SEM

image of the electrode, showing the distribution of NWs along the PEDOT:PSS layer.

The porous layer consists of PDMS (matrix) with different ratios of NH₄HCO₃. The NH₄HCO₃ is an inorganic compound consisting of nitrogen, carbon, oxygen, and hydrogen. Upon heating, NH₄HCO₃ is decomposed into carbon dioxide (CO₂), ammonia (NH₃), and water (H₂O). So, after printing the porous dielectric the device was placed in a preheated oven for 1 h at 90 °C to allow the formation of pores. Equation (1) illustrates the decomposition of the annealed NH₄HCO₃ at 90 °C via an endothermic process:



Furthermore, PDMS is an excellent biocompatible material and PDMS fluids can degrade in the environment as the clay minerals in the soil hydrolyze the PDMS into dimethylsilanediol (DMSD), which can either biodegrade or evaporate in the environment. In the atmosphere, DMSD oxidizes in the presence of sunlight. In both of the cases, the end products of DMSD degradation are H₂O, SiO₂, and CO₂.^[57] Additionally, PDMS has no adverse effect on terrestrial or aquatic organisms.^[58]

3.1. Effect of Different Ratios on Porous PDMS

Figure 3a,b shows microscopic images of pore sizes and distribution and a histogram with pore diameters for different porous layers. When the ratio was changed, the pore sizes altered as well. As the images in Figure 3a depict, the pore size is inversely proportional to the ratio of PDMS:NH₄HCO₃. Pores in the D1 image are quite larger than pores in images D2 and D3. In the D1 layer, salt compounds have more space for the release of CO₂ and form bubbles. This can be attributed to the D1 layer, in which salt compounds have more space for the release of CO₂ and form bubbles. In D2 layers, in which salt compounds occupied greater

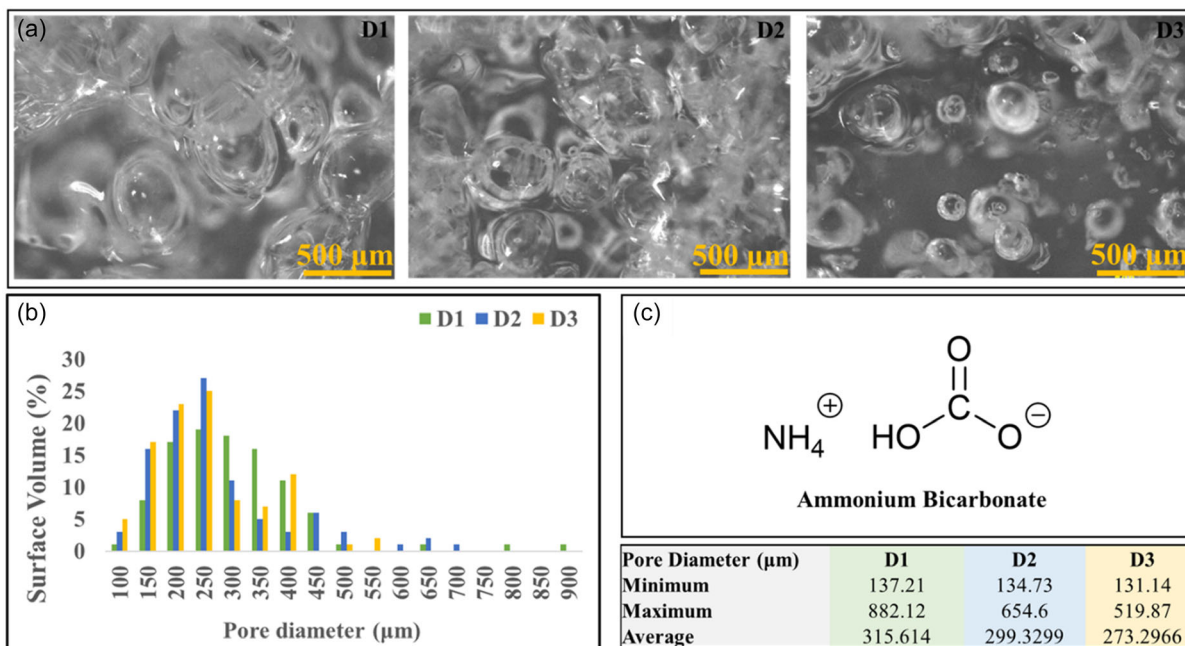


Figure 3. a) Microscopic images with a pore distribution and b) histogram with pore size on different porous layers with a ratio of PDMS:NH₄HCO₃, D1 (4:0.8), D2 (4:1), and D3 (4:1.2) and c) molecular structure of NH₄HCO₃. The table shows minimum, maximum, and average pore diameters for the three porous layers.

surface area, smaller bubbles were formed. In D2 and D3, the number of pores in relation to the total volume of the porous layer (porosity) was much lower than in the layer of D1.

The histogram in Figure 3b confirms that the formation of pores is affected by the concentration of NH₄HCO₃ in the PDMS matrix. All the devices showed varying range of pore diameters. However, D1 had the broadest range starting from 137.21 to 882.12 μm, while D2 and D3 consisted of pores diameters of 134.73–654.6 μm and 131.14–519.87 μm, respectively. Even though the minimum pore size in all cases is approximately the same, the average diameter is the one that matters because it clearly demonstrates the difference in the pore size of each device. D1 has pores with 10% and 15% larger diameters than D2 and D3.

Table 1 outlines the main features for each porous dielectric layer. The thickness of each layer was measured with slide calipers with an error of ±0.2 mm. It is also noticed that porosity influences the thickness of the dielectric layer. Device D1 with the largest pores had the thickest dielectric layer. The dielectric constant (ϵ_r) was calculated following Equation (2). Capacitance was measured for all devices in the frequency range 1 Hz to 1 MHz. The capacitance value corresponding to 1 kHz (2.068, 2.91, and 3.595 pF for the porous layer with ratios 4:0.8, 4:1, and 4:1.2, respectively) was used in Equation (2) to calculate each dielectric constant. Based on these values, the dielectric constants were found as 1.246, 1.388, and 1.498 for the layers with composition ratios 4:0.8, 4:1, and 4:1.2, respectively. The value of ϵ_r for the porous PDMS (4:0.8) is relatively lower than the other two cases because the pores within the PDMS matrix are larger due to the trapped gasses, and thus the porosity is higher. In general, layers with higher porosity lead to lower ϵ_r .^[4]

$$C = \epsilon_{\text{air}} \epsilon_r \frac{A}{d} \quad (2)$$

where ϵ_{air} is the permittivity of air ($8.85 \times 10^{-12} \text{ F m}^{-1}$), ϵ_r is the relative permittivity of the dielectric layer, A is the overlapped area of the two electrodes, and d is the distance between the two electrodes.

3.2. Capacitive Response: Effect of Different Ratios of Porous PDMS

Figure 4a–c demonstrates the relative change of capacitance under stepwise loadings for the three devices (D1, D2, and D3). Device D1 can perform almost the same way when various pressure loads are applied and unloaded. Device D2 also exhibited quite similar outputs; however, the relative change of capacitance is not the same, and it looks unstable, when the pressure in the range 0–50 kPa was unloaded. As for device D3, it is clear that this device is not operating similarly during the loading and unloading conditions.

The devices were also characterized for their response under a range of applied pressure until they saturate (Figure 4d–f). The applied pressure started at 5 kPa and ended when variations were not detected for all devices. Each pressure value was applied for approximately 10 s. For device D1, changes were observed until the applied pressure reached 170 kPa. The variations for device D2 were noticeable up to 210 kPa with some noises. The capacitance of device D2 changed until the applied pressure reached 190 kPa. The variations in the capacitances of D2 and D3 were negligible for high pressures (170–210 kPa). On the other hand, device D1 showed more linear responses at a larger pressure range. Also, Figure 4f shows that the response of D3 in

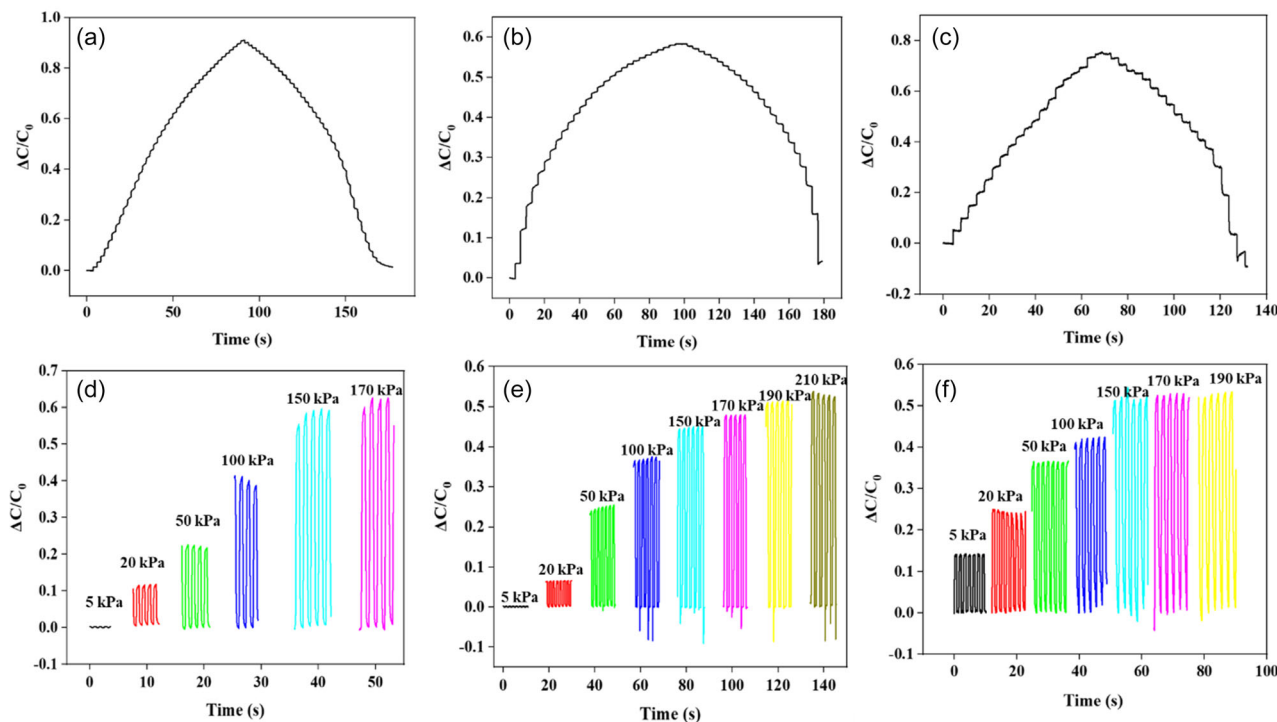


Figure 4. a–c) Stepwise response under different pressure ranges for devices D1, D2, and D3, respectively. d–f) Dynamic response under different pressure ranges for devices D1, D2, and D3.

100–170 kPa range was relatively unstable with greater noise. The limited values of capacitance change for D2 and D3 reveal that for high pressures (170–210 kPa), there is possibly no space for the pores to be compressed further. Besides, as D2 and D3 are less porous (stiffer–higher dielectric constants), they are deformed comparatively less than the more porous (softer–lower dielectric constant) D1.

Figure 5 illustrates the corresponding relative capacitance change when a range of pressures were applied on the three devices. The device D1 exhibited a linear response ($R^2 = 0.99$) in the pressure range of 0–170 kPa with a sensitivity of 0.0055 kPa^{-1} . In contrast, devices D2 and D3 showed three different linear ranges. **Figure 6b** shows that the device D2 works in three different pressure ranges: 0–100 kPa ($R^2 = 0.95$), 100–170 kPa ($R^2 = 0.98$), and 170–210 kPa ($R^2 = 0.99$) with respective sensitivity of

0.0027 kPa^{-1} . **Figure 5c** shows that device D3 corresponds to different linear ranges of 0–130 kPa ($R^2 = 0.88$) and 150–190 kPa ($R^2 = 0.99$) with sensitivity of 0.0041 kPa^{-1} . The nonlinear responses of the devices D2 and D3 could be attributed to the mechanical properties of their respective porous dielectric layers. Their higher pressure range and lower sensitivity can be attributed to the Young’s modulus of the dielectric layers, as shown in **Figure S4**, Supporting Information. The tensile stress–strain analysis revealed the dielectric layer having Young’s modulus of 224.9 kPa for D1, while D2 and D3 showed values of 256.91 and 309.44 kPa, respectively. These findings provide additional support for the relationship between mechanical properties and sensitivity. By increasing the porosity of the dielectric layer, the mechanical properties (softness) get improved and the sensitivity of the device is enhanced.^[4]

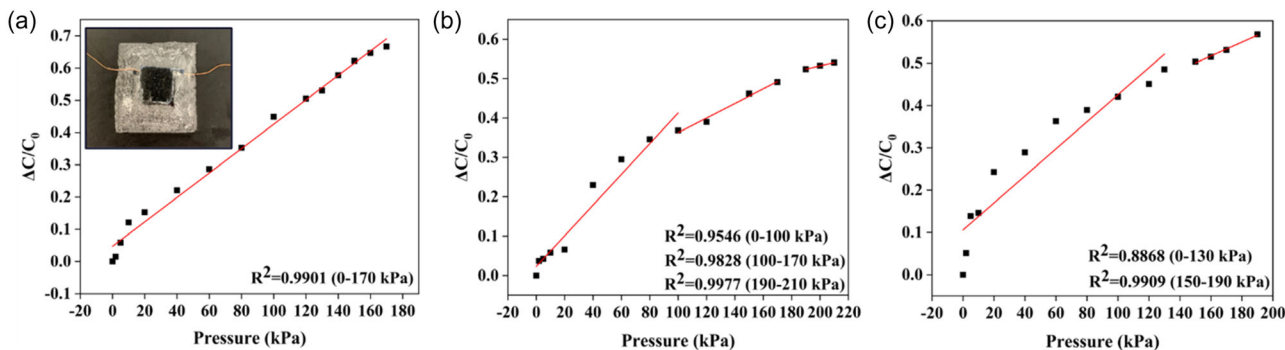


Figure 5. Responses under different pressures for devices a) D1, inset image: 3D printed device, b) D2, and c) D3.

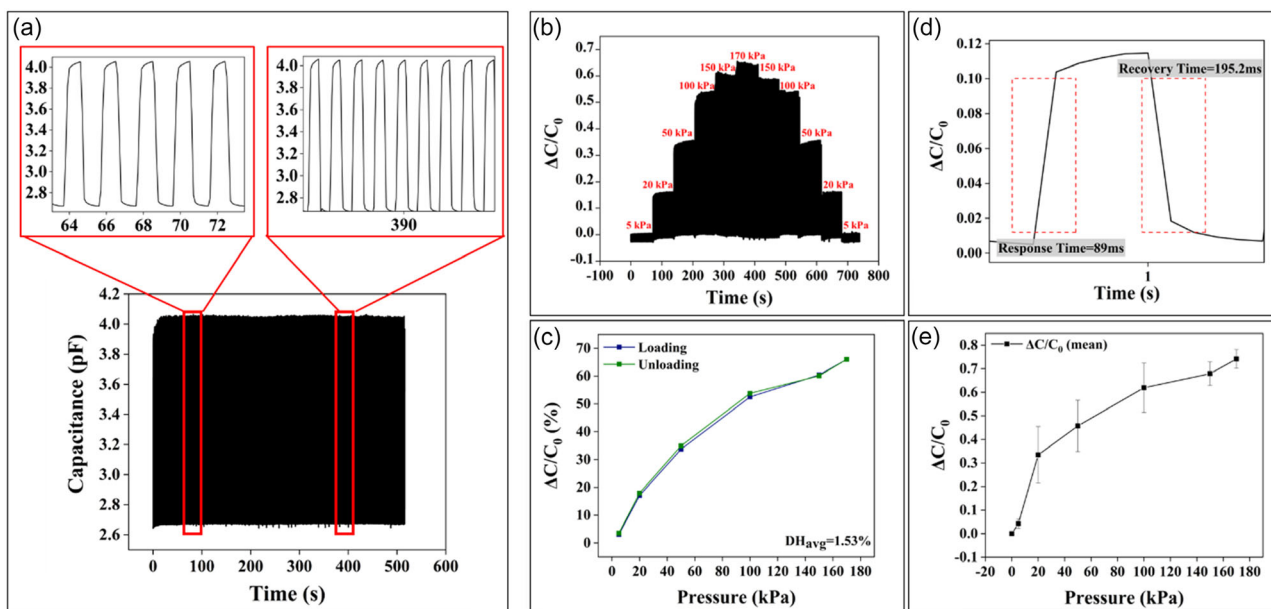


Figure 6. a) Stability, b) stepwise stability, c) hysteresis, and d) response and recovery time upon loading/unloading of 20 kPa for the device D1 and e) mean values of relative capacitance of five D1 sensors under the same pressure range 5–170 kPa.

Table S1, Supporting Information, compares various pressure sensors using porous PDMS as the dielectric layer and Table S2, Supporting Information, compares pressure sensors fabricated with different printing techniques including fused deposition modeling (FDM) and selective laser sintering (SLS). From both tables, it is observed that the DIW-fabricated device (D1) demonstrates comparable sensitivities in most cases and outperforms others with significantly lower hysteresis and faster response times. The low hysteresis of D1 ensures greater accuracy during cyclic loading. The fast response time of these devices can be useful for real-time monitoring in dynamic applications. While higher sensitivities (ranging from 0.36 to 1.12 MPa⁻¹) have been reported for some other works, it is crucial to consider the overall sensor performance.^[4,47] The effectiveness of a pressure sensor relies not only on the sensitivity but also on other factors such as hysteresis and response time, as they collectively determine the real-world applicability. Reduced hysteresis and response time can significantly enhance the overall performance of the sensor.

3.3. Hysteresis Response and Repeatability

The capacitive responses for three devices confirmed that device D1 exhibited a stable response under a wide applied pressure range with high linearity and sensitivity. Thus, device D1 was selected as the optimized capacitive pressure sensor for further characterizations. The stability of the sensor was evaluated by subjecting the device to cyclic loading (loading 3 s and unloading 3 s) for 500 cycles. Figure 6a shows that the capacitive response was almost the same for all cycles, indicating the excellent repeatability. The internal figures illustrate the response for 70–100 and 385–415 cycles with maximum capacitance 4.051 and 4.055 pF, respectively. The base capacitances for both cycle ranges were 2.6701 and 2.674 pF for 70–100 and 385–415 cycles. Therefore, it can be assumed that the sensor is highly stable.

The stability of the sensor was also assessed under large loading–unloading cycles by applying stepwise pressures from 5 to 170 kPa and then reducing it back to 5 kPa. The pressure was applied on the sensor for 5 min (loading 3 s and unloading 3 s). Figure 6b illustrates the repeatability of the sensor for all the loading–unloading pressures. The sensor response obtained by maximum capacitance for each loading step is shown in Figure 6c. The hysteresis was calculated for each pair of pressures using Equation (3). The average hysteresis was found to be 1.53%:

$$DH(\%) = \frac{C_2 - C_1}{C_p - C_b} \times 100 \quad (3)$$

where C_2 and C_1 are the capacitances during unloading and loading, respectively, C_p is the maximum capacitance (at 170 kPa), and C_b is the base capacitance (at 0 kPa).

The response and recovery time of the sensor are depicted in Figure 6d. The response time was calculated as 89 ms when 20 kPa was loaded on the sensor. The recovery time was found to be approximately 195.2 ms.

The uniformity of five D1 sensors was evaluated for the pressure range 5–170 kPa. The standard deviation of the mean relative change of capacitance was calculated for each applied pressure, as shown in Figure 6e, and the results showed that the variation in sensor responses is noticeable in the pressure range of 20–100 kPa. The variation was negligible for higher pressures. This could be attributed to the varying porosities of each dielectric layer, which decides the volume of air. Additionally, factors such as the thickness of the dielectric layer may also contribute to the variations in sensor responses. The results suggest that the sensors have uniform response at higher pressures. These findings are important for understanding the limitations and potential sources of variability in the performance of the D1 sensors.

3.4. Comparison with Pristine PDMS as the Dielectric Layer

The porous PDMS sensor was compared with bulk PDMS-based sensor. Figure S5, Supporting Information, illustrates the capacitive response and stability of the two sensors when a range of pressures was applied. Figure S5a, Supporting Information, shows that the pristine PDMS-based sensor's operating range only reaches 100 kPa while the porous-based devices work functionally well at least up to 170 kPa. It is also noticeable from Figure S5b, Supporting Information, that the pristine PDMS-based sensor shows some drift in the response during longer operation time (500 cycles), along with some noises. Figure S5c, Supporting Information, illustrates the linearity and sensitivity of the device. It was found that the sensor has relatively poorer sensitivity of 0.0043 kPa^{-1} which is approximately 30% less sensitive than device D1. Moreover, its capacitive responses exhibit relatively poorer linearity ($R^2 = 0.88992$). This result can be given to the mechanical properties of the dielectric layers. These results can be explained by the higher Young's modulus of PDMS (1.67 MPa) compared to the porous PDMS (224.9 kPa). The device based on a pristine PDMS layer is not as deformable as the one with porous PDMS.^[45]

4. Application Demonstration

4.1. Underwater Pressure Sensing

The performance of the printed capacitive pressure sensor was also examined in a water environment, as pressure feedback

could be used to control the movement of robots at defined depths. In this case, the sensing layer was isolated from the water by enclosing the sensor with bulk PDMS. The sensor was dipped in a water container (filled with tap water up to a depth of 60 cm), as shown in Figure 7a. The sensor is connected to the LCR meter via copper wires and the change in capacitance value is recorded using the LabVIEW interface. The packaged sensor was dipped in steps of 10 cm and the observed response is shown in Figure 7b. An increase in the capacitance value was observed with depth. This is due to the compression of the sensor by water pressure and the change in dielectric constant due to varying pores (137.21–882.12 μm). The obtained response displays a stable sensing performance at each defined water level. Video S1, Supporting Information, shows the underwater pressure sensing performance of the sensor. The sensor exhibits a nearly linear response ($\Delta C/C_0$) in the range 2.7–18.3 for 10–60 cm depth, as shown in Figure 7c. The observed response shows the suitability of the fabricated sensor for underwater pressure monitoring applications. Also, the sensor displayed the ability to return to its base capacitance value after it was removed from the water container, as shown in Figure 7b. Further, Figure 7d shows that the device has negligible hysteresis (1.33%). The cyclic repeatability (for five cycles) performance of the sensor was also determined at each water level (i.e., 10, 20, 30, 40, 50, and 60 cm), as displayed in Figure 7e. The obtained results show almost similar performance during five loading/unloading cycles. The response stability analysis was also carried out by observing the underwater sensing response continuously for 50 loading/unloading cycles at 60 cm depth, as shown in Figure 7f. The obtained results

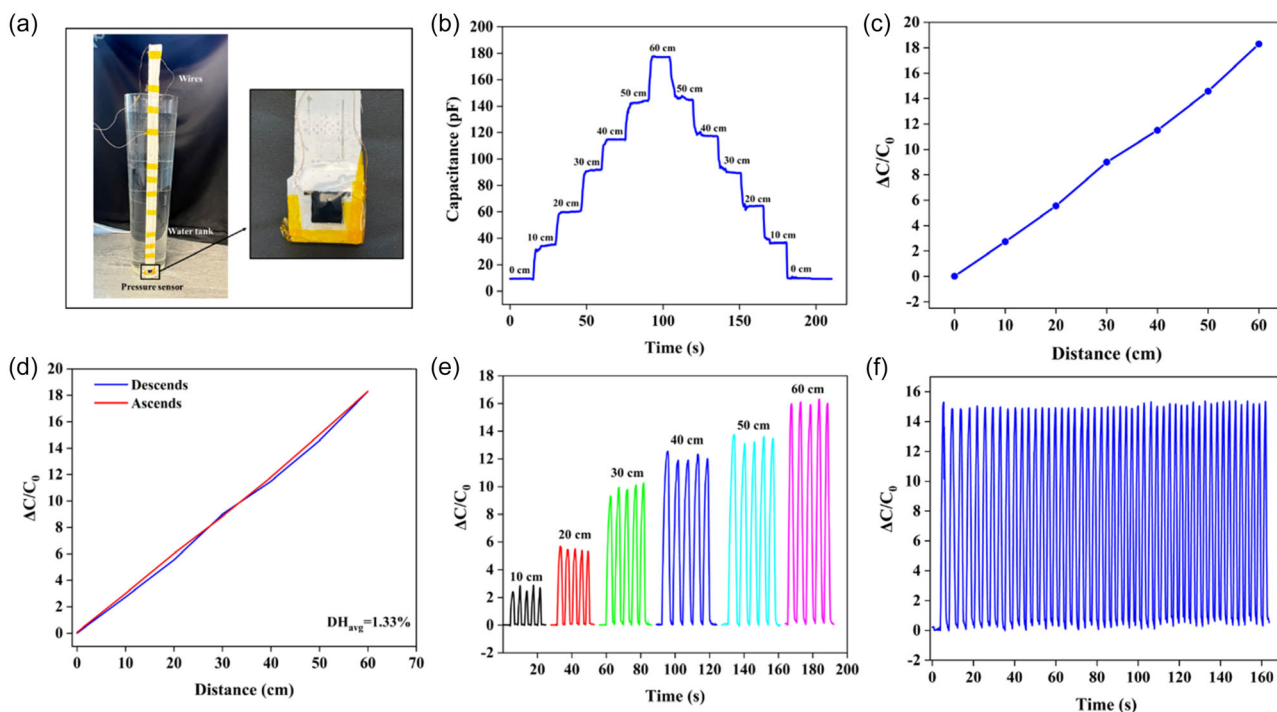


Figure 7. a) Fabricated pressure sensor dipped in a water tank. b) Stepwise response of the sensor up to 60 cm depth. c) Response ($\Delta C/C_0$) versus water depth graph. d) Hysteresis analysis graph. e) Five-cyclic repeatability analysis at different water levels. f) Response stability analysis through 50 loading/unloading cycles at 60 cm depth.

indicate highly stable and repeatable behavior of the sensor toward underwater pressure monitoring.

4.2. Pressure Mapping for Shape Measuring

To further demonstrate the potential use of presented sensors in e-skin, the 2×2 and 3×3 matrix arrays were developed. Each sensor on the array has dimension of $10 \text{ mm} \times 10 \text{ mm}$. On application of external pressure on 2×2 array matrix we noted clearly distinguishable response from each sensor, as shown in Video S2, Supporting Information. With 3×3 array, we were able to use the pressure map to discern the object shapes, such as a concentric circle, the letter L, and the number 7 (Video S2, Supporting Information). These demonstrations show the scalability of presented approach and the practical applications of presented sensors in fields such as robotics, human-machine interfaces, and wearables.

5. Conclusion

A DIW-based approach for multimaterial 3D printed capacitive pressure sensors is presented. The DIW is an attractive method owing to good dimensional control, ease of scaling up, and the potential to manufacture devices with complex shapes. The effect of different concentrations of NH_4HCO_3 on the porosity of PDMS was analyzed. The results suggest that the device fabricated using PDMS: NH_4HCO_3 of 4:0.8 showed a wide linear working range of 5–170 kPa with a sensitivity of 0.0055 kPa^{-1} . Several devices were tested for response uniformity and some variation was observed in the pressure range 5–100 kPa. However, the response is uniform at higher pressures values. The comparison of porous PDMS with pristine PDMS-based devices confirmed the superior performance of the former. Considering these features, the presented sensors also offer attractive end-of-life solutions as they will not contribute to electronic waste. Finally, the demonstration of developed sensors for underwater pressure sensing and object shape identification confirms their potential use in applications such as monitoring human motion, underwater vehicles, and robotics.

The capacitive pressure sensors based on porous PDMS can suffer from nonuniformity due to variations in the pore size, dimensional variations, and the composition of materials. One way to address the nonuniformity is to use a thin-film technique to deposit a conductive layer on top of the porous PDMS surface. Another approach is to use multiple sensing elements in the sensor design. By using multiple sensing elements, the sensor can average out any nonuniformity in the porous PDMS material, resulting in a more accurate and reliable measurement. It is important to carefully design the sensor and control the fabrication process to ensure that the porous PDMS material is as uniform as possible. This can be achieved by carefully controlling the fabrication parameters such as curing time and temperature. Future efforts will focus on improving the uniformity of device response as well as resolution. Finally, a detailed investigation related to degradability of presented sensors and qualitative analysis of end product will be explored as future work.

Supporting Information

Supporting Information is available from the Wiley Online Library or from the author.

Acknowledgements

This work was supported in part by the Engineering and Physical Sciences Research Council through Engineering Fellowship for Growth (grant no. EP/R029644/1) and Heteroprint Program Grant (grant no. EP/R03480X/1). The work was initiated by R.D.'s Bendable Electronics and Sensing Technologies (BEST) Group when he was at University of Glasgow, UK. The work got completed after he moved to Northeastern University, USA, where his group is known as Bendable Electronics and Sustainable Technologies (BEST) Group. X.K. thanks Dr. Morteza Amjadi Koulour for providing the lab facility for the tensile stress-strain testing and the Ph.D. student Tom Jacquin for assisting in the characterization.

Conflict of Interest

The authors declare no conflict of interest.

Author Contributions

X.K.: Conceptualization, methodology, writing—original draft. G.K.: Validation, methodology, writing—review and editing. A.B.: Underwater pressure sensing application section (experimental part and writing—original draft and review/editing). R.C.: Data curation (pressure mapping). P.S.: Supervision, review and editing. R.D.: Conceptualization, methodology, supervision, writing—review and editing, project administration.

Data Availability Statement

The data that support the findings of this study are available from the corresponding author upon reasonable request.

Keywords

additive manufacturing, capacitive sensors, direct ink writing, porous polydimethylsiloxane (PDMS), pressure sensors, soft sensors

Received: June 29, 2023

Revised: August 27, 2023

Published online:

- [1] F. Liu, S. Deswal, A. Christou, Y. Sandamirskaya, M. Kaboli, R. Dahiya, *Sci. Rob.* **2022**, *7*, eabl7344.
- [2] A. Paul, N. Yogeswaran, R. Dahiya, *Adv. Intell. Syst.* **2022**, *4*, 2200183.
- [3] O. Ozioko, R. Dahiya, *Adv. Intell. Syst.* **2022**, *4*, 2100091.
- [4] S. Masihi, M. Panahi, D. Maddipatla, A. J. Hanson, A. K. Bose, S. Hajian, V. Palaniappan, B. B. Narakathu, B. J. Bazuin, M. Z. Atashbar, *ACS Sens.* **2021**, *6*, 938.
- [5] M. Ntagios, R. Dahiya, *IEEE Sens. J.* **2022**, <https://doi.org/10.1109/JSEN.2022.3179233>.
- [6] O. Ozioko, P. Karipoth, P. Escobedo, M. Ntagios, A. Pullanchiyodan, R. Dahiya, *Adv. Intell. Syst.* **2021**, *3*, 1900145.
- [7] Y. Kumaresan, S. Mishra, O. Ozioko, R. Chirila, R. Dahiya, *Adv. Intell. Syst.* **2022**, *4*, 2200043.
- [8] P. Karipoth, A. Pullanchiyodan, A. Christou, R. Dahiya, *ACS Appl. Mater. Interfaces* **2021**, *13*, 61610.

- [9] S. Jung, J. H. Kim, J. Kim, S. Choi, J. Lee, I. Park, T. Hyeon, D. H. Kim, *Adv. Mater.* **2014**, *26*, 4825.
- [10] C. L. Choong, M. B. Shim, B. S. Lee, S. Jeon, D. S. Ko, T. H. Kang, J. Bae, S. H. Lee, K. E. Byun, J. Im, *Adv. Mater.* **2014**, *26*, 3451.
- [11] N. Yogeswaran, E. S. Hosseini, R. Dahiya, *ACS Appl. Mater. Interfaces* **2020**, *12*, 54035.
- [12] C. Dagdeviren, Y. Su, P. Joe, R. Yona, Y. Liu, Y.-S. Kim, Y. Huang, A. R. Damadoran, J. Xia, L. W. Martin, Y. Huang, J. A. Rogers, *Nat. Commun.* **2014**, *5*, 4496.
- [13] W. Choi, J. Lee, Y. Kyoung Yoo, S. Kang, J. Kim, J. Hoon Lee, *Appl. Phys. Lett.* **2014**, *104*, 123701.
- [14] S. Ma, Y. Kumaresan, A. S. Dahiya, L. Lorenzelli, R. Dahiya, *IEEE Sens. J.* **2022**, <https://doi.org/10.1109/JSEN.2022.3140651>.
- [15] A. Petropoulou, S. Kralj, X. Karagiorgis, I. Savva, E. Loizides, M. Panagi, T. Krasia-Christoforou, C. Riziotis, *Sci. Rep.* **2020**, *10*, 367.
- [16] G. Min, Y. Xu, P. Cochran, N. Gadegaard, D. M. Mulvihill, R. Dahiya, *Nano Energy* **2021**, *83*, 105829.
- [17] K. Y. Lee, H.-J. Yoon, T. Jiang, X. Wen, W. Seung, S.-W. Kim, Z. L. Wang, *Adv. Mater.* **2016**, *6*, 1502566.
- [18] J.-H. Son, D. Heo, Y. Song, J. Chung, B. Kim, W. Nam, P. T. J. Hwang, D. Kim, B. Koo, J. Hong, S. Lee, *Nano Energy* **2022**, *93*, 106797.
- [19] G. Min, A. S. Dahiya, D. M. Mulvihill, R. Dahiya, in *2021 IEEE Int. Conf. on Flexible and Printable Sensors and Systems (FLEPS)*, IEEE, Piscataway, NJ **2021**, pp. 1–4.
- [20] G. Khandelwal, R. Dahiya, *Adv. Mater.* **2022**, *34*, 2200724.
- [21] Y. Kumaresan, S. Ma, O. Ozioko, R. Dahiya, *IEEE Sens. J.* **2022**, *22*, 3974.
- [22] K. F. Lei, K.-F. Lee, M.-Y. Lee, *Microelectron. Eng.* **2012**, *99*, 1.
- [23] B. Narakathu, A. Eshkeiti, A. Reddy, M. Rebros, E. Rebrosova, M. Joyce, B. Bazuin, M. Atashbar, in *2012 IEEE Sensors*, IEEE, Piscataway, NJ **2012**, pp. 1–4.
- [24] F. Nikbakhtnasrabadi, E. S. Hosseini, S. Dervin, D. Shakhivel, R. Dahiya, *Adv. Electron. Mater.* **2022**, *8*, 2101348.
- [25] J. I. Yoon, K. S. Choi, S. P. Chang, *Microelectron. Eng.* **2017**, *179*, 60.
- [26] O. Ozioko, W. Navaraj, M. Hersh, R. Dahiya, *Sensors* **2020**, *20*, 4780.
- [27] F. Xu, X. Li, Y. Shi, L. Li, W. Wang, L. He, R. Liu, *Micromachines* **2018**, *9*, 580.
- [28] Z. He, W. Chen, B. Liang, C. Liu, L. Yang, D. Lu, Z. Mo, H. Zhu, Z. Tang, X. Gui, *ACS Appl. Mater. Interfaces* **2018**, *10*, 12816.
- [29] L. Zhang, S. Zhang, C. Wang, Q. Zhou, H. Zhang, G.-B. Pan, *ACS Sens.* **2021**, *6*, 2630.
- [30] P. Escobedo, M. Ntagios, D. Shakhivel, W. T. Navaraj, R. Dahiya, *IEEE Trans. Rob.* **2020**, *37*, 683.
- [31] S.-W. Dai, Y.-L. Gu, L. Zhao, W. Zhang, C.-H. Gao, Y.-X. Wu, S.-C. Shen, C. Zhang, T.-T. Kong, Y.-T. Li, L.-X. Gong, G.-D. Zhang, L.-C. Tang, *Composites, Part B* **2021**, *225*, 109243.
- [32] A. Abedi, M. Hasanzadeh, L. Tayebi, *Mater. Chem. Phys.* **2019**, *237*, 121882.
- [33] E. S. Hosseini, S. Dervin, P. Ganguly, R. Dahiya, *ACS Appl. Bio Mater.* **2020**, *4*, 163.
- [34] X. Karagiorgis, M. Ntagios, P. J. Skabara, R. Dahiya, *IEEE J. Flexible Electron.* **2023**, *2*, 175.
- [35] S. H. Kim, J.-H. Moon, J. H. Kim, S. M. Jeong, S.-H. Lee, *Biomed. Eng. Lett.* **2011**, *1*, 199.
- [36] J. Hwang, Y. Kim, H. Yang, J. H. Oh, *Composites, Part B* **2021**, *211*, 108607.
- [37] Y. Kumaresan, O. Ozioko, R. Dahiya, *IEEE Sens. J.* **2021**, *21*, 26243.
- [38] R. Dahiya, W. T. Navaraj, S. Khan, E. O. Polat, *Inf. Disp.* **2015**, *31*, 6.
- [39] Y. Long, X. Zhao, X. Jiang, L. Zhang, H. Zhang, Y. Liu, H. Zhu, *FlatChem* **2018**, *10*, 1.
- [40] B. You, C. J. Han, Y. Kim, B.-K. Ju, J.-W. Kim, *J. Mater. Chem. A* **2016**, *4*, 10435.
- [41] D. A. John, C. Parameswaran, S. Sandhu, R. Dahiya, *IEEE Sens. Lett.* **2023**, *7*, 2501104.
- [42] E. S. Hosseini, M. Chakraborty, J. Roe, Y. Petillot, R. S. Dahiya, *IEEE Sens. J.* **2022**, *22*, 9914.
- [43] W. Li, X. Jin, X. Han, Y. Li, W. Wang, T. Lin, Z. Zhu, *ACS Appl. Mater. Interfaces* **2021**, *13*, 19211.
- [44] W. Kaiqiang, L. Xingyang, *Mater. Res. Express* **2020**, *7*, 105003.
- [45] L. Dan, S. Shi, H.-J. Chung, A. Elias, *ACS Appl. Nano Mater.* **2019**, *2*, 4869.
- [46] M. Amit, R. K. Mishra, Q. Hoang, A. M. Galan, J. Wang, T. N. Ng, *Mater. Horiz.* **2019**, *6*, 604.
- [47] S. W. Park, P. S. Das, J. Y. Park, *Org. Electron.* **2018**, *53*, 213.
- [48] Q. Wang, A. Chen, H. Gu, G. Qin, J. Zhang, J. Xu, G. Jiang, W. Liu, Z. Zhang, H. Huang, *J. Mater. Sci.* **2021**, *56*, 11723.
- [49] C. Parameswaran, D. Gupta, *J. Mater. Chem. C* **2018**, *6*, 5473.
- [50] S. Dervin, E. S. Hosseini, R. Dahiya, in *2021 IEEE Int. Conf. on Flexible and Printable Sensors and Systems (FLEPS)*, IEEE, Piscataway, NJ **2021**, pp. 1–4.
- [51] S. Masihi, M. Panahi, D. Maddipatla, A. K. Bose, X. Zhang, A. J. Hanson, V. Palaniappan, B. B. Narakathu, B. J. Bazuin, M. Z. Atashbar, in *2019 IEEE Sensors*, IEEE, Montreal, QC, Canada **2019**, 1–4.
- [52] N. Yuan, C. Wang, J. Ji, K. Zhou, *J. Mater. Sci.: Mater. Electron.* **2021**, *32*, 27656.
- [53] J. Cárdenas-Martínez, B. L. España-Sánchez, R. Esparza, J. A. Ávila-Niño, *Synth. Met.* **2020**, *267*, 116436.
- [54] N. Liu, G. Fang, J. Wan, H. Zhou, H. Long, X. Zhao, *J. Mater. Chem.* **2011**, *21*, 18962.
- [55] G. A. Sarabi, M. Latifi, R. Bagherzadeh, *AIP Conf. Proc.* **2018**, *1920*, 020045.
- [56] P. Patil, S. Patil, P. Kate, A. A. Kulkarni, *Nanoscale Adv.* **2021**, *3*, 240.
- [57] E. F. C. Griessbach, R. G. Lehmann, *Chemosphere* **1999**, *38*, 1461.
- [58] N. J. Fendinger, in *Organosilicon Chemistry IV: From Molecules to Materials* (Eds: N. Auner, J. Weis), Wiley-VCH, Weinheim **2000**, Ch. 103, pp. 626–638, <https://doi.org/10.1002/9783527619917.ch103>.